forward peak in Fig. 2', and hence the side peaks in the TOF profiles in Fig. 1. Analysis of the angular distributions showed that the time-delayed mechanism is also mainly responsible for the sideways ridge (see Fig. 2), and hence for the broadening of the TOF profiles around $E = 1.4-1.7$ eV.

We see that the HD product from the time-delayed mechanism starts to form at scattering angles of roughly 45°, where the wavefunction is found to have mostly 'high impact parameter' components, corresponding to $J = 15-20$. This indicates that the H atoms that react via this mechanism come from the parts of the plane wave (green function in Fig. 3) around $R\sin\theta = \pm(1.1-1.6)$ bohr. It is likely therefore that H attacks the D_2 at a glancing angle, in contrast to the direct mechanism (in which H attacks the D_2 bond collinearly). If this happens, then energy initially concentrated in the HDD bend must be converted into energy along the HDD asymmetric stretch, to allow the system to pass over the transition state and react.

The successful combination of experiment and theory to elucidate in detail the mechanisms involved in one of the simplest chemical reactions, the hydrogen exchange reaction, can also be applied to more complex reactions. These include the reactions $O(^1D) + H_2 \rightarrow OH + H$, $F + HD \rightarrow HF + D$, and $H + H_2O \rightarrow OH + H_2$, for which experimental angular distributions and realistic potential energy surfaces are available[19,20], and for which it is computationally feasible to solve the time-dependent Schrödinger equation. □

1. Hirshfelder, J. O., Eyring, H. & Topley, B. Reactions involving hydrogen molecules and atoms. *J. Chem. Phys.* **4,** 170–177 (1936).
2. Truhlar, D. G. & Wyatt, R. E. History of H₃ kinetics. *Annu. Rev. Phys. Chem.* **27,** 1–43 (1976).
3. Neuhauser, D. *et al.* State-to-state rates for the D + H₂(v = 1,j = 1) → HD(v′,j′) + H reaction–predictions and measurements. *Science* **257,** 519–522 (1992).
4. Boothroyd, A. I., Keogh, W. J., Martin, P. G. & Peterson, M. R. A refined H₃ potential surface. *J. Chem. Phys.* **104,** 7139–7152 (1996).
5. Zhang, J. Z. H. & Miller, W. H. Quantum reactive scattering via the S-matrix version of the Kohn variational principle: integral cross sections for H + H₂(v₁ = j₁ = 0) → H₂(v₂ = 1,j₂ = 1,3) + H in the energy range E_total = 0.9-1.4 eV. *Chem. Phys. Lett.* **153,** 465–470 (1988).
6. Miller, W. H. Recent advances in quantum mechanical reactive scattering theory. *Annu. Rev. Phys. Chem.* **41,** 245–281 (1990).
7. D'Mello, M., Manolopoulos, D. E. & Wyatt, R. E. Quantum dynamics of the H + D₂ → D + HD reaction: comparison with experiment. *J. Chem. Phys.* **94,** 5985–5993 (1991).
8. Aoiz, F. J., Herrero, V. J. & Sáez Rábanos, V. Quasiclassical state to state reaction cross sections for D + H₂(v = 0,j = 0) → HD(v′,j′) + H. Formation and characteristics of short-lived collision complexes. *J. Chem. Phys.* **97,** 7423–7436 (1992).
9. Miller, W. H. & Zhang, J. Z. H. How to observe the elusive resonances in H or D + H₂ → H₂ or HD + H reactive scattering. *J. Phys. Chem.* **95,** 12–19 (1991).
10. Schatz, G. C. & Kuppermann, A. Dynamical resonances in collinear, coplanar, and three-dimensional quantum mechanical reactive scattering. *Phys. Rev. Lett.* **35,** 1266–1269 (1973).
11. Skodje, R. T., Sadeghi, R., Köppel, H. & Krause, J. L. Spectral quantization of transition state dynamics for the three-dimensional H + H₂ reaction. *J. Chem. Phys.* **101,** 1725–1729 (1994).
12. Allison, T. C., Friedman, R. S., Kaufman, D. J. & Truhlar, D. G. Analysis of the resonance in H + D₂ → HD(v′ = 3) + D. *Chem. Phys. Lett.* **327,** 439–445 (2000).
13. Fernández-Alonso, F. & Zare, R. N. Scattering resonances in the simplest chemical reaction. *Annu. Rev. Phys. Chem.* **53,** 67–99 (2002).
14. Nieh, J.-C. & Valentini, J. J. Experimental observation of dynamical resonances in the H + H₂ reaction. *Phys. Rev. Lett.* **60,** 519–522 (1988).
15. Schnieder, L., Seekamp-Rahn, K., Wrede, E. & Welge, K. H. Experimental determination of quantum state resolved differential cross sections for the hydrogen exchange reaction H + D₂ → HD + D. *J. Chem. Phys.* **107,** 6175–6195 (1997).
16. Wrede, E. *et al.* The dynamics of the hydrogen exchange reaction at 2.20 eV collision energy: comparison of experimental and theoretical differential cross sections. *J. Chem. Phys.* **110,** 9971–9981 (1999).
17. Fernández-Alonso, F., Bean, B. D. & Zare, R. N. Differential cross sections for H + D₂ → HD(v′ = 1,J′ = 1,5,8) + D at 1.7 eV. *J. Chem. Phys.* **111,** 1035–1042 (1999).
18. Fernández-Alonso, F., Bean, B. D. & Zare, R. N. Differential cross sections for H + D₂ → HD(v′ = 2,J′ = 0,3,5) + D at 1.55 eV. *J. Chem. Phys.* **111,** 2490–2498 (1999).
19. Liu, K. Crossed-beam studies of neutral reactions: state-specific differential cross sections. *Annu. Rev. Phys. Chem.* **52,** 139–164 (2001).
20. Casavecchia, P. Chemical reaction dynamics with molecular beams. *Rep. Prog. Phys.* **63,** 355–414 (2000).
21. Fernández-Alonso, F. *et al.* Evidence for scattering resonances in the H + D₂ reaction. *Angew. Chem. Int. Edn Engl.* **39,** 2748–2752 (2000).
22. Fernández-Alonso, F. *et al.* Forward scattering in the H + D₂ → HD + D reaction: comparison between experiment and theoretical predictions. *J. Chem. Phys.* **115,** 4534–4545 (2001).
23. Zewail, A. H. Femtochemistry: atomic-scale dynamics of the chemical bond. *J. Phys. Chem.* **104,** 5660–5694 (2000).
24. Rinnen, K.-D., Buntine, M. A., Kliner, D. A. V., Zare, R. N. & Huo, W. M. Quantitative determination of H₂, HD, and D₂ internal-state distributions by (2+1) resonance-enhanced multiphoton ionization. *J. Chem. Phys.* **95,** 214–225 (1991).
25. Althorpe, S. C. Quantum wavepacket method for state-to-state reactive cross sections. *J. Chem. Phys.* **114,** 1601–1616 (2001).
26. Skouteris, D., Castillo, J. F. & Manolopoulos, D. E. ABC: a quantum reactive scattering program. *Comput. Phys. Commun.* **133,** 128–135 (2000).
27. Althorpe, S. C., Kouri, D. J. & Hoffman, D. K. Further partitioning of the reactant-product decoupling equations of state-to-state reactive scattering and their solution by the time-independent wavepacket method. *J. Chem. Phys.* **107,** 7816–7824 (1997).
28. Judson, R. S., Kouri, D. J., Neuhauser, D. & Baer, M. Time-dependent wavepacket method for the complete determination of S-matrix elements for molecular reactive collisions in 3 dimensions. *Phys. Rev. A* **42,** 351–366 (1990).
29. Balint-Kurti, G. G., González, A. I., Goldfield, E. M. & Gray, S. K. Quantum reactive scattering of O(¹D) + H₂ and O(¹D) + HD. *Faraday Discuss.* **110,** 169–183 (1998).
30. Huang, Y., Zhu, W., Kouri, D. J. & Hoffman, D. K. Distributed approximating function approach to atom-diatom reactive scattering: Time-dependent and time-independent wavepacket treatments. *J. Phys. Chem.* **98,** 1868–1874 (1994).

....

Glacial–interglacial stability of ocean pH inferred from foraminifer dissolution rates

David M. Anderson* **& David Archer**†

* *NOAA Paleoclimatology Program and University of Colorado, 325 Broadway, Boulder, Colorado 80303, USA*

† *Department of Geophysical Sciences, University of Chicago, 5734 S. Ellis Ave., Chicago, Illinois 60637, USA*

....

The pH of the ocean is controlled by the chemistry of calcium carbonate. This system in turn plays a large role in regulating the CO_2 concentration of the atmosphere on timescales of thousands of years and longer. Reconstructions of ocean pH and carbonate-ion concentration are therefore needed to understand the ocean's role in the global carbon cycle. During the Last Glacial Maximum (LGM), the pH of the whole ocean is thought to have been significantly more basic[1], as inferred from the isotopic composition of boron incorporated into calcium carbonate shells, which would partially explain the lower atmospheric CO_2 concentration at that time. Here we reconstruct carbonate-ion concentration—and hence pH—of the glacial oceans, using the extent of calcium carbonate dissolution observed in foraminifer faunal assemblages as compiled in the extensive global CLIMAP data set[2]. We observe decreased carbonate-ion concentrations in the glacial Atlantic Ocean, by roughly 20 μmol kg⁻¹, while little change occurred in the Indian and Pacific oceans relative to today. In the Pacific Ocean, a small (5 μmol kg⁻¹) increase occurred below 3,000 m. This rearrangement of ocean pH may be due to changing ocean circulation from glacial to present times, but overall we see no evidence for a shift in the whole-ocean pH as previously inferred from boron isotopes[1].

Foraminifer assemblage alteration by preferential dissolution has been recognized since the earliest studies in micropalaeontology. After the temperature of the surface environment, dissolution is the next most important variable in explaining the distribution of foraminifer faunas on the sea floor. Most foraminifer palaeotemperature equations identify a 'dissolution factor' that strongly correlates with water depth and isolates the variance due to dissolution as statistically independent from the variation due to sea surface temperature. Other factors include productivity[3] and surface ocean mixed-layer depth[4]. The dominant species in the dissolution factor are typically *Globigerinoides sacculifer*, *Neogloboquadrina dutertrei*, *Pulleniatina obliquiloculata*, *Globorotalia menardii* and *Globorotalia tumida*[5]. The effect of carbonate ion saturation is apparent in plots of *N. dutertrei*, *Globigerinoides ruber* and *Globigerina bulloides* species abundance (%) versus carbonate-ion saturation and sea surface temperature (Fig. 1). In addition to the dominant correlation with temperature, these and other species have a less dramatic but statistically robust association with carbonate-ion content. The greatest abundance of *N. dutertrei* is found only in the environment where temperature is warm and the sea floor is undersaturated. Likewise, *G. bulloides*, most abundant in water of 8–12 °C, is less abundant in supersaturated environments and more abundant in undersaturated environments.
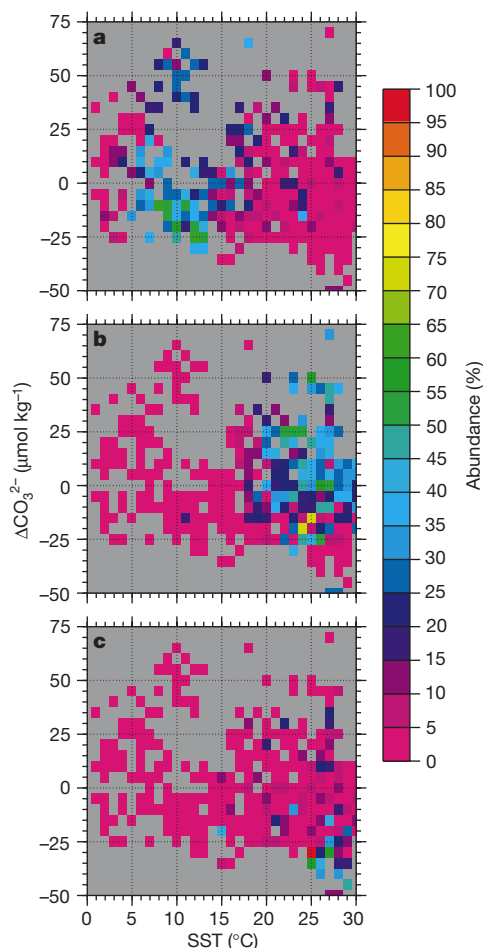
We reconstructed the saturation state of calcite, ΔCO_3^{2-}, of the glacial ocean from the global CLIMAP[5] planktonic foraminifer abundance data set, using the modern analogue technique (see Methods). A data set of core-top species counts, coupled with modern deep-ocean ΔCO_3^{2-} values, provides the calibration. A test assemblage is compared with core-top data to find its five closest modern analogues. The mean of the analogue ΔCO_3^{2-} values provides the estimate of the test ΔCO_3^{2-}. The scatter in analogue ΔCO_3^{2-} provides an estimate of the uncertainty, which is generally 10 μmol kg^{-1} or less. The same method has been used to estimate sea surface temperatures, to within 1.5 °C (ref. 5).

We calculated the absolute carbonate-ion concentration, $[CO_3^{2-}] = \Delta CO_3^{2-} + CO_{3sat}^{2-}$ (refs 6, 7) and averaged the observations across 500-m depth intervals for the Atlantic ($n = 163$) and combined Indian and Pacific ($n = 108$) samples (Fig. 2). The data are shown in the context of calcite saturation (heavy solid line) and the mean $[CO_3^{2-}]$ and its standard deviation σ (light solid line and dashed envelope). The reconstructions reproduce both the mean and the scatter of the observed water column distributions of $[CO_3^{2-}]$. Each point is typically the average of at least ten samples (that is, fifty analogues) except for the two shallowest glacial Atlantic averages where $n = 4$.

The largest difference in the glacial ocean is in the Atlantic. Today freshly ventilated North Atlantic Deep Water (NADW), high in CO_3^{2-}, distinguishes the chemistry of the Atlantic from the Pacific and Indian oceans. According to palaeotracers [13]C (ref. 8) and Cd (ref. 9) there existed a glacial analogue of NADW (GNADW), which ventilated the water column to about 2.3-km depth[10,11]. The intermediate Pacific[12,13] and Indian[14] oceans were also apparently more ventilated than today. In addition, the glacial decrease in atmos-

Figure 1 Foraminifer abundance in core-top sediments versus sea surface temperature and carbonate-ion saturation at the sea floor. Abundance (%) for three species (**a**, *Globigerina bulloides*; **b**, *Globigerinoides ruber*; and **c**, *Neoglobquadrina dutertrei*) from the core-top database of 905 samples are shown as a function of mean annual sea surface temperature (SST) and the carbonate-ion saturation (ΔCO_3^{2-}) corresponding to the water depth of the sample.
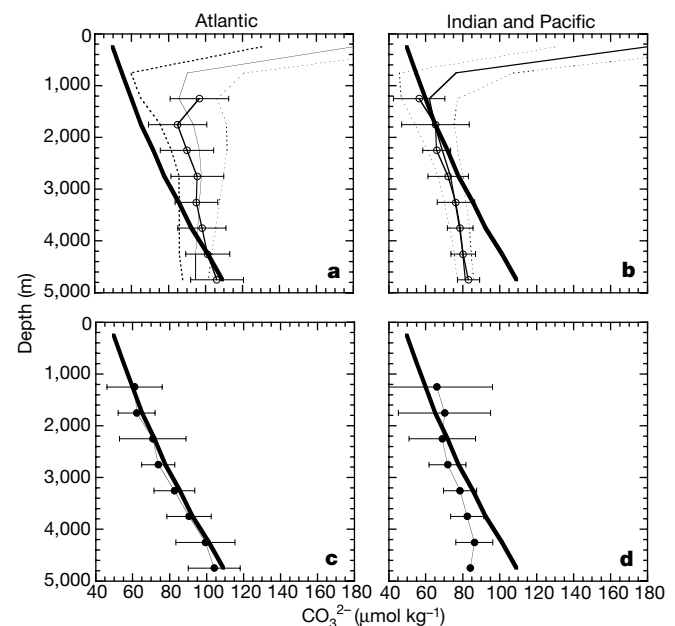

Figure 2 Vertical profiles of carbonate-ion concentration in the modern and glacial Atlantic and combined Indian and Pacific oceans. Modern estimates for the Atlantic (**a**) and Indian and Pacific (**b**) reconstructed from core-top samples ($n = 905$) averaged for 500-m depth intervals (open circles), are compared with the average (thin solid line) and range (dashed line, one standard deviation above and below the mean) in concentration from the modern gridded database, and with the saturation profile (thick line). Reconstructions for the Last Glacial Maximum for the Atlantic (**c**) ($n = 163$) and Indian and Pacific (**d**) ($n = 108$) averaged for 500-m depth intervals (filled circles) relative to saturation (thick line) for the Atlantic and the combined Indian and Pacific ocean samples. The uncertainty is the standard deviation of the CO_3^{2-} of all selected analogues for each 500-m depth interval.
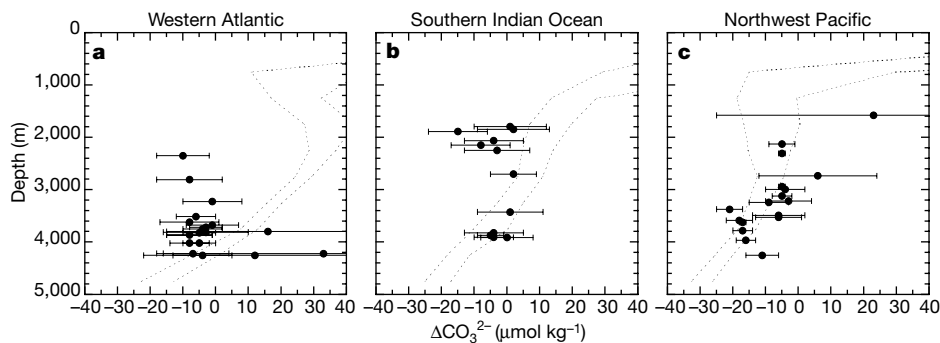
Figure 3 Vertical profiles of carbonate-ion saturation (ΔCO_3^{2-}) in three regions for the modern and Last Glacial Maximum. **a**, Western Atlantic (30° S–10° N, 30–60° W). **b**, Southern Indian Ocean (60–20° S, 70–120° E). **c**, Northwest Pacific (10–50° N, 120° E to 150° W). The range in ΔCO_3^{2-} observed today in each region is shown by the dashed lines marking one standard deviation above and below the regional mean. Each LGM estimate (filled circle) is derived from the ΔCO_3^{2-} associated with the five closest modern analogue samples, determined using the squared-chord dissimilarity measure. The uncertainty in LGM estimates is the standard deviation in ΔCO_3^{2-} of the five closest modern analogs.

pheric p_{CO_2}, well documented in ice cores, demands a glacial increase in CO_3^{2-}, at least at the sea surface. The low values of CO_3^{2-} that we observe at intermediate depths throughout all three basins are therefore puzzling. Perhaps the method breaks down in supersaturated intermediate waters, but there is no evidence for this in our internal tests of the modern data set (see Methods). Transport of CO_2 through the atmosphere, or dissolution of $CaCO_3$, can decouple CO_3^{2-} from nutrients (and the palaeotracers listed above). Given the difficulty of explaining the mechanism behind the low p_{CO_2} of the glacial atmosphere[15], we are reluctant to dismiss the apparently robust data presented here.

Regional reconstructions from the western Atlantic, the southern Indian Ocean, and the northwest Pacific are presented in Fig. 3. The changes are largest in the Western Atlantic, where ΔCO_3^{2-} decreased from 20 to zero or −10 between 2,000 and 4,000 m. The decrease in CO_3^{2-} made the Atlantic more corrosive across a broad depth range, consistent with other observations of reduced preservation relative to today. There is some indication that ΔCO_3^{2-} in deep water (>4,000 m) increased, but the standard deviation of the deep estimates are large. A similar pattern occurred in the southern Indian Ocean, where saturation decreased to around zero above 3,000 m relative to today, and increased slightly (5 μmol) at 4,000 m relative to present. The ΔCO_3^{2-} changes were small in the northwest Pacific. Above 3,000 m, any change is within 1σ of present conditions. Below 3,000 m, several samples indicate that ΔCO_3^{2-} was increased, and a few samples indicate little change. The glacial carbonate-ion reconstruction is consistent with the established picture of enhanced preservation in the glacial Pacific relative to today, and reduced preservation in the glacial Atlantic[16–20].

In general, our results appear to be inconsistent with the boron-isotope estimate that CO_3^{2-} at 3.5 km in the Pacific was 100 μmol higher than today[1]; instead they imply that CO_3^{2-} changed little during LGM except in the Atlantic. It is possible that a change in the relative rain rates of organic carbon and calcite might have shifted the lysocline relative to the saturation horizon[21], shifting also the

present relationship between dissolution intensity and ΔCO_3^{2-} that we rely on here. However, the relationship between dissolution intensity and ΔCO_3^{2-} in core-top samples is robust across broad geographic regions, and we do not suppose that such a systematic relationship could have changed so uniformly. Analogous objections to the rain ratio hypothesis have been raised based on the tight relationship between the saturation horizon and the calcium carbonate distribution (CCD) today[22]. The absence of a CO_3^{2-} change points to sea-floor $CaCO_3$ as an effective buffer of ocean pH on the ~10-kyr timescales of the glacial–interglacial cycles. □

Methods

Carbonate-ion saturation

To estimate carbonate-ion saturation for a sample, we used the modern analogue technique to find the five samples in a modern database of 905 core-top samples that are most similar with regard to faunal composition as measured by the squared chord dissimilarity[23], using the 29 species common to the foraminifer equations used by CLIMAP[5]. The carbonate-ion saturation for each core-top sample was interpolated at the depth the core was taken from the gridded database produced by Archer[22]. We averaged the carbonate-ion saturation at the locations of the top five analogues to obtain the estimated carbonate-ion value (see example in Table 1). The principle that allows use to reconstruct both temperature and CO_3^{2-} is the observation that unique faunas are associated with discrete combinations of CO_3^{2-} and temperature. For example, a simplified case with only a few species, a fossil sample originating in a cold surface and undersaturated sea-floor environment (perhaps consisting of 100% *Neogloboquadrina pachyderma* left coiling) would find analogues (containing 100% *N. pachyderma*) from a similar environment in the core-top database (cold and undersaturated), and would be dissimilar to all core-top samples from cold-surface, saturated sea-floor environments (perhaps containing *Globigerina quinquiloba*, or other cold-water but dissolution-susceptible species in addition to *N. pachyderma*). Unlike transfer functions that attribute all the variation to one forcing variable, methods like the modern analogue technique are appropriate for relationships between (multivariate) species abundance and multivariate forcing influences.

Accuracy tests

The accuracy of the reconstructed carbonate-ion saturation can be evaluated in several ways. We compared expected and observed carbonate-ion saturation for the core-top database: $n = 905$; $r = 0.85$; standard error, 11 μmol kg^{-1}; comparable to the root-mean-square (r.m.s) uncertainty between the gridded CO_3^{2-} data and the ungridded data from which it was constructed. A second test is to compare reconstructed versus observed mean ΔCO_3^{2-} profiles for the Atlantic and combined Indian and Pacific oceans. In Fig. 2, the open circles are reconstructed using faunal analogues, and the light solid line is the area-weighted average for the gridded water-column data. The agreement is everywhere within 10 μmol kg^{-1}, and the analogue technique is even able to reproduce some of the observed variability in CO_3^{2-}. Third, we reconstructed ΔCO_3^{2-} for modern core-top samples not included in the calibration. The five closest analogues for one such modern core-top sample (RC12-113) are listed in Table 1. The observed 0 μmol kg^{-1} ΔCO_3^{2-} at the RC12-113 site is very close to the −2 μmol kg^{-1} ΔCO_3^{2-} mean of the five analogues.

Measured changes in species abundance

Changes in species abundance above the saturation horizon are more subtle than are

Table 1 Modern analogues for sample RC12-113

Analog sample ID	Dissimilarity	Depth (m)	ΔCO_3^{2-} (μmol kg^{-1})
V14-81	0.08	3,634	−1
V21-108	0.09	1,900	−2
V28-309	0.09	2,166	0
RC12-365	0.11	2,787	−4
V21-107	0.13	2,217	−4
Mean	0.10	2,540	−2

Sample obtained from 0–1 cm (core-top) in the southern Coral Sea, modern ΔCO_3^{2-} 0 μmol kg^{-1}.

observed below, but even above the saturation horizon, observable variations in species abundance can be attributed to subsurface respiration-driven dissolution, which is expected to be influenced by the overlying water ΔCO_3^{2-} (ref. 24). If carbonate-ion saturation had no effect on foraminifer abundance above the lysocline, we would expect a larger standard deviation in ΔCO_3^{2-} for estimates above the lysocline because faunally similar samples should be associated with a wider range of saturation levels. No such trend in the standard deviation is observed, supporting our assumption that faunal patterns above the lysocline are also associated with narrow ($10\,\mu mol\,kg^{-1}$) ranges of ΔCO_3^{2-}. We note that the method seems to work in spite of regional variation in respiration-driven dissolution. Either these differences must be relatively small, or they are correlated with faunal assemblage.

Constraints on the method

In addition to the limitations of the method imposed by the uncertainty of the estimate, there are additional limitations imposed by the CLIMAP and modern analogue databases. From both the core-top and the CLIMAP LGM data sets, most of the samples are concentrated in the middle water column, with fewer at extreme high or low ΔCO_3^{2-} values. There are few core-top samples with ΔCO_3^{2-} higher than $+60\,\mu mol\,kg^{-1}$, so we limit our reconstruction to samples deeper than 1,000 m, where we expect the ΔCO_3^{2-} to remain below $50\,\mu mol\,kg^{-1}$. Most of the CLIMAP LGM samples lie between 2,000–4,000 m.

1. Sanyal, A., Hemming, N. G., Hanson, N. & Broecker, W. S. Evidence for a higher pH in the glacial ocean from boron isotopes in foraminifera. *Nature* **373**, 234–236 (1995).
2. CLIMAP Project Members. Seasonal reconstruction of the Earth's surface at the last glacial maximum. *Geol. Soc. Am. Map Chart Ser.* **MC-36**, 1–18 (1981).
3. Mix, A. C. Influence of productivity variations on long-term atmospheric CO_2. *Nature* **337**, 541–544 (1989).
4. Ravelo, A. C., Fairbanks, R. G. & Philander, S. G. H. Reconstructing topical Atlantic hydrography using planktonic foraminifera and an ocean model. *Paleoceanography* **5**, 409–431 (1990).
5. Prell, W. L. The stability of low-latitude sea-surface temperatures: An evaluation of the CLIMAP reconstruction with emphasis on the positive SST anomalies. (Report TR025, Department of Energy, Washington DC, 1985).
6. Millero, F. J. The effect of pressure on the solubility of minerals in water and seawater. *Geochim. Cosmochim. Acta* **46**, 11–22 (1982).
7. Mucci, A. The solubility of calcite and aragonite in seawater at various salinities, temperatures, and one atmosphere total pressure. *Am. J. Sci.* **283**, 780–799 (1983).
8. Duplessey, J. C. *et al.* Deep water source variations during the last climatic cycle and their impact on the global deep water circulation. *Paleoceanography* **3**, 343–360 (1988).
9. Oppo, D. W. & Horowitz, M. Glacial deep water geometry: South Atlantic benthic foraminiferal Cd/Ca and $\delta^{13}C$ evidence. *Paleoceanography* **15**, 147–160 (2000).
10. Yu, E.-F., Bacon, M. P. & Francois, R. Similar rates of modern and last glacial ocean thermohaline circulation inferred from radiochemical data. *Nature* **379**, 689–694 (1996).
11. Winguth, A., Archer, D. & Maier-Reimer, E. in *Inverse Methods in Global Biogeochemical Cycles* (eds Kasibhatla, P. *et al.*) (AGU Press, Washington DC, 2000).
12. Kennett, J. P. & Ingram, B. L. A 20,000 year record of ocean circulation and climate change from the Santa Barbara Basin. *Nature* **377**, 510–514 (1995).
13. Ganeshram, R. S., Pedersen, T. F., Calvert, S. E. & Murray, J. W. Large changes in oceanic nutrient inventories from glacial to interglacial periods. *Nature* **376**, 755–758 (1995).
14. Altabet, M. A., Francoise, R., Murray, D. M. & Prell, W. L. Climate-related variations in denitrification in the Arabian Sea from sediment $^{15}N/^{14}N$ ratios. *Nature* **373**, 506–509 (1995).
15. Archer, D., Winguth, A., Lea, D. & Mahowald, N. What caused the glacial/interglacial atmospheric pCO_2 cycles? *Rev. Geophys.* **38**, 159–189 (2000).
16. Farrell, J. W. & Prell, W. L. Climate change and $CaCO_3$ preservation: an 800,000 year bathymetric reconstruction from the central equatorial Pacific Ocean. *Paleoceanography* **4**, 447–466 (1989).
17. Peterson, L. C. & Prell, W. L. in *The Carbon Cycle and Atmospheric Carbon Dioxide: Natural Variations Archean to Present* (eds Sundquist, E. T. & Broecker, W. S.) 251–269 (American Geophysical Union, Washington DC, 1985).
18. Curry, W. B. & Lohmann, G. P. in *The Carbon Cycle and Atmospheric Carbon Dioxide: Natural Variations Archean to Present* (eds Sundquist, E. T. & Broecker, W. S.) 285–301 (American Geophysical Union, Washington DC, 1985).
19. Howard, W. R. & Prell, W. L. Late Quaternary $CaCO_3$ production and preservation in the Southern Ocean: Implications for oceanic and atmospheric carbon cycling. *Paleoceanography* **9**, 453–482 (1994).
20. Crowley, T. J. in *The Carbon Cycle and Atmospheric Carbon Dioxide: Natural Variations Archean to Present* (eds Sundquist, E. T. & Broecker, W. S.) 271–284 (American Geophysical Union, Washington DC, 1985).
21. Archer, D. & Maier-Reimer, E. Effect of deep-sea sedimentary calcite preservation on atmospheric CO_2 concentration. *Nature* **367**, 260–263 (1994).
22. Archer, D. An atlas of the distribution of calcium carbonate in deep sea sediments. *Glob. Biogeochem. Cycles* **10**, 159–174 (1996).
23. Overpeck, J. T., Webb, T. & Prentice, I. C. Quantitative interpretation of fossil pollen spectra: dissimilarity coefficients and the method of modern analogs. *Quat. Res.* **23**, 87–108 (1985).
24. Emerson, S. & Bender, M. L. Carbon fluxes at the sediment water interface of the deep sea: Calcium carbonate preservation. *J. Mar. Res.* **39**, 139–162 (1981).

....

Laser–Raman imagery of Earth's earliest fossils

J. William Schopf*, Anatoliy B. Kudryavtsev†, David G. Agresti†, Thomas J. Wdowiak† & Andrew D. Czaja*

* *Department of Earth & Space Sciences, and Institute of Geophysics & Planetary Physics (Center for the Study of the Evolution and Origin of Life), University of California, Los Angeles, California 90095-1567, USA*
† *Astro and Solar System Physics Program, Department of Physics, University of Alabama at Birmingham, Birmingham, Alabama 35294-1170, USA*

....

Unlike the familiar Phanerozoic history of life, evolution during the earlier and much longer Precambrian segment of geological time centred on prokaryotic microbes[1]. Because such microorganisms are minute, are preserved incompletely in geological materials, and have simple morphologies that can be mimicked by nonbiological mineral microstructures, discriminating between true microbial fossils and microscopic pseudofossil 'lookalikes' can be difficult[2,3]. Thus, valid identification of fossil microbes, which is essential to understanding the prokaryote-dominated, Precambrian 85% of life's history, can require more than traditional palaeontology that is focused on morphology. By combining optically discernible morphology with analyses of chemical composition, laser–Raman spectroscopic imagery of individual microscopic fossils provides a means by which to address this need. Here we apply this technique to exceptionally ancient fossil microbe-like objects, including the oldest such specimens reported from the geological record, and show that the results obtained substantiate the biological origin of the earliest cellular fossils known.

Over the past few decades, the rules for accepting ancient microfossil-like objects as *bona fide* Precambrian fossils have become well established. Such objects should be demonstrably biogenic, and indigenous to and syngenetic with the formation of rocks of known provenance and well-defined Precambrian age[2,4,5]. Of these criteria, the most difficult to satisfy has proved to be biogenicity, in particular for the notably few fossil-like objects reported from Archaean ($>2,500$ million years (Myr) old) deposits[2,4]—the putative biological origin of which has been beset by controversy[2,6–8]. This difficulty has been obviated in part by analyses of the isotopic composition of carbon in coexisting inorganic (carbonate) minerals and in whole-rock acid-resistant carbonaceous residues (kerogens), which have been used to trace the isotopic signature of biological (photoautotrophic) carbon fixation to at least $\sim3,500$ Myr ago[9]. But because investigations of such bulk kerogen samples yield only an average value of the materials analysed, they cannot provide information about the biogenicity of individual minute objects that are claimed to be fossil.

Significant progress toward solving this problem has been made by using an ion microprobe to analyse the carbon isotopic composition of single Precambrian microfossils[10]. Laser–Raman spectroscopic imagery of ancient individual fossil microbes provides a means by which to extend available analytical data to a molecular level. In a previous study[11], we applied this technique to analyses *in situ* of Eocene fossil wood and Precambrian microscopic organic-walled fossils, and showed that it can provide insight into the molecular make-up and the fidelity of preservation of the kerogenous matter of which such fossils are composed. Because Raman spectroscopy is non-intrusive, non-destructive and particularly sensitive to the distinctive carbon signal of carbonaceous (kerogenous) organic matter, it is an ideal technique for such studies. Here we have used this technique to investigate graphitic, geochemically highly altered, dark brown to black carbonaceous filaments that have been inferred to be remnants of especially